AGU PUBLICATIONS

Geophysical Research Letters

RESEARCH LETTER

10.1002/2016GL070469

Key Points:
- We construct geoelectric hazard maps using solid-earth impedances and magnetic observatory data
- Results summarize extreme-event 100 year amplitude of storm-time geoelectric fields
- This work is motivated by power-grid industry needs and United States space weather strategic plans

Correspondence to:
J. J. Love,
jlove@usgs.gov

Citation:
Love, J. J., et al. (2016), Geoelectric hazard maps for the continental United States, *Geophys. Res. Lett.*, *43*, 9415–9424, doi:10.1002/2016GL070469.

Received 15 JUL 2016
Accepted 1 SEP 2016
Accepted article online 5 SEP 2016
Published online 19 SEP 2016

©2016. The Authors.
This is an open access article under the terms of the Creative Commons Attribution-NonCommercial-NoDerivs License, which permits use and distribution in any medium, provided the original work is properly cited, the use is non-commercial and no modifications or adaptations are made.

Geoelectric hazard maps for the continental United States

Jeffrey J. Love[1], Antti Pulkkinen[2], Paul A. Bedrosian[3], Seth Jonas[4], Anna Kelbert[1], E. Joshua Rigler[1], Carol A. Finn[1], Christopher C. Balch[5], Robert Rutledge[5], Richard M. Waggel[6], Andrew T. Sabata[7], Janet U. Kozyra[8], and Carrie E. Black[8]

[1]Geomagnetism Program, U.S. Geological Survey, Denver, Colorado, USA, [2]NASA Goddard Space Flight Center, Greenbelt, Maryland, USA, [3]Crustal Geophysics and Geochemistry Science Center, U.S. Geological Survey, Denver, Colorado, USA, [4]Science and Technology Policy Institute, Institute for Defense Analyses, Washington, District of Columbia, USA, [5]NOAA Space Weather Prediction Center, Boulder, Colorado, USA, [6]Office of Energy Infrastructure Security, Federal Energy Regulatory Commission, Washington, District of Columbia, USA, [7]Federal Emergency Management Agency, Denton, Texas, USA, [8]National Science Foundation, Arlington, Virginia, USA

Abstract In support of a multiagency project for assessing induction hazards, we present maps of extreme-value geoelectric amplitudes over about half of the continental United States. These maps are constructed using a parameterization of induction: estimates of Earth surface impedance, obtained at discrete geographic sites from magnetotelluric survey data, are convolved with latitude-dependent statistical maps of extreme-value geomagnetic activity, obtained from decades of magnetic observatory data. Geoelectric amplitudes are estimated for geomagnetic waveforms having 240 s sinusoidal period and amplitudes over 10 min that exceed a once-per-century threshold. As a result of the combination of geographic differences in geomagnetic activity and Earth surface impedance, once-per-century geoelectric amplitudes span more than 2 orders of magnitude and are an intricate function of location. For north-south induction, once-per-century geoelectric amplitudes across large parts of the United States have a median value of 0.26 V/km; for east-west geomagnetic variation the median value is 0.23 V/km. At some locations, once-per-century geoelectric amplitudes exceed 3 V/km.

1. Introduction

Geoelectric fields are induced in the Earth's electrically conducting crust, lithosphere, mantle, and ocean by natural time-dependent geomagnetic field variations that are generated by dynamic processes in the Earth's surrounding space weather environment. This induction occurs all the time, during both calm and stormy conditions. But during intense magnetic storms, induced geoelectric fields can drive quasi-direct currents in bulk electric-power grids of sufficient strength to interfere with their operation, sometimes causing blackouts and damaging transformers [e.g., *Molinski*, 2002; *Thomson*, 2007; *Piccinelli and Krausmann*, 2014]. Historically, the most dramatic realization of this natural hazard occurred in March 1989 [e.g., *Allen et al.*, 1989], when an intense magnetic storm caused the collapse of the entire Hydro-Québec electric-power grid in Canada [*Bolduc*, 2002; *Béland and Small*, 2005]. Years earlier, in August 1972, a magnetic storm that was, by most measures, of modest global intensity induced geoelectric fields that interrupted the operation of a major telecommunications cable running between Plano, Illinois, and Cascade, Iowa [*Anderson et al.*, 1974]. More recently, the Halloween magnetic storm of October 2003 induced measurable currents in power-grid systems in Scotland [*Thomson et al.*, 2005] and caused operational failures in grid systems in Sweden [*Pulkkinen et al.*, 2005].

According to some scenario analyses, the future occurrence of an extremely intense magnetic storm might result in continental-scale failure of electric-power grids [e.g., *Cannon et al.*, 2013], and the associated negative consequences for society could be long lasting [e.g., *Baker et al.*, 2008; *Kappenman*, 2012]. Recognizing a need for mitigating measures, in May 2013, the United States Federal Energy Regulatory Commission [*Federal Energy Regulatory Commission*, 2013] (Order No. 779) issued a directive to the North American Electric Reliability Corporation (NERC) to develop reliability standards to address the impact of geomagnetic disturbances on the bulk power system. As a part of this process, NERC developed preliminary geoelectric benchmarks for intense magnetic storms [*NERC*, 2014] using surface impedances derived from simple one-dimensional Earth conductivity models of undetermined accuracy.

In support of a multiagency project for assessing induction hazards [e.g., *Love et al.*, 2014; *Pulkkinen*, 2015], we map extreme-value geoelectric amplitudes over large portions of the continental United States. We construct our maps using a data-derived ("empirical") parameterization of induction—convolving a latitude-dependent statistical map of ground-level geomagnetic activity with surface impedances measured at discrete geographic locations during magnetotelluric surveys. This work is consistent with priorities established by the United States National Science and Technology Council [*National Science and Technology Council*, 2015] (Goal 1.1) and related international initiatives [*Schrijver et al.*, 2015] for pursuing induction-hazard research. The results presented here inform both hazard assessments and the development of real-time hazard mapping projects. Our maps of storm-time geoelectric amplitudes can be used to evaluate induction hazards for power grids [e.g., *Overbye et al.*, 2012; *Burstinghaus et al.*, 2013; *Zheng et al.*, 2013; *Torta et al.*, 2014]. They also inform United States Department of Energy [e.g., *Veeramany et al.*, 2016] and private sector [e.g., *Aon Benfield*, 2013; *Lloyd's*, 2013] projects for assessing risks for power-grid systems associated with magnetic storms.

2. Induction

Our interest, here, is with ground-level geomagnetic activity $\mathbf{B}(t, x, y)$, a function of time t and geographic location (x, y), and the induced surface geoelectric variation $\mathbf{E}(t, x, y)$. Under Fourier transformation from the time domain to the frequency domain,

$$\mathcal{F}\{\mathbf{B}(t)\} = \mathbf{B}(\omega) \quad \text{and} \quad \mathcal{F}\{\mathbf{E}(t)\} = \mathbf{E}(\omega), \tag{1}$$

where for a sinusoid with period T, the angular frequency is $\omega = 2\pi/T$. If space weather activity is assumed to be far above the Earth's surface, then geomagnetic activity realized at the Earth's surface can be approximated as occurring in the local horizontal plane, and we can reasonably focus attention on horizontal geomagnetic (north B_x, east B_y) and geoelectric (E_x, E_y) components. Furthermore, in the "low-frequency" limit, Maxwell's displacement current can be ignored. Under these and other simplifying assumptions [e.g., *Simpson and Bahr*, 2005, chap. 2.1], the laws of Ampère, Faraday, and Ohm that govern induction in an electrically conducting medium [e.g., *Stratton*, 1941, chap. 5] can be summarized in terms of a linear equation; for horizontal geomagnetic $\mathbf{B}_h(\omega, x, y)$ and geoelectric $\mathbf{E}_h(\omega, x, y)$ field components,

$$\mathbf{E}_h(\omega, x, y) = \frac{1}{\mu}\mathbf{Z}(\omega, x, y; \sigma(\mathbf{r})) \cdot \mathbf{B}_h(\omega, x, y), \tag{2}$$

where μ is magnetic permeability, assumed to be the free-space constant. The impedance tensor $\mathbf{Z}$ has units of ohms (Ω); it is a function of frequency and location, and it has a nonlinear dependence on the three-dimensional (3-D) electrical conductivity structure $\sigma(\mathbf{r})$ (or, equivalently, the resistivity $\rho = 1/\sigma$) within the volume ($\mathbf{r}$ is position vector) of the Earth; the response function $\mathbf{Z}/\mu$ has units of (V/km)/nT. For a given geomagnetic activity $\mathbf{B}_h$, through the impedance $\mathbf{Z}$ tensor, the 3-D conductivity structure of the Earth $\sigma(\mathbf{r})$ affects the local amplitude, polarization, and phase of the induced geoelectric field.

The vector-tensor equation (2) can be compared and contrasted with the scalar equation used by *NERC* [2014, equation II.3] to characterize once-per-century peak geoelectric amplitude,

$$E_N(\lambda, x, y) \simeq 8 \cdot \alpha(\lambda) \cdot \beta(x, y) \quad \text{(V/km)}. \tag{3}$$

This equation was derived for an assumed time domain peak geoelectric amplitude; it has no explicit frequency dependence, and it has no notion of polarization or phase; α spans 0.1 to 1.0, depending on geomagnetic latitude λ [*NERC*, 2014, Table II-1], and β spans 0.21 to 1.17, depending on the convolution of a geomagnetic waveform like that of the March 1989 storm with surface impedance obtained from a one-dimensional (1-D) Earth conductivity model for designated physiographic (geological) regions in the United States and Canada [*NERC*, 2014, Table II-2].

3. Empirical and Model Impedances

Magnetotellurics is a science concerned with the estimation of solid-earth electrical conductivity structure from surface measurements of geomagnetic and geoelectric variations [e.g., *Simpson and Bahr*, 2005; *Unsworth*, 2007]. Since 2006, the National Science Foundation has supported a national-scale magnetotelluric

survey in the United States, through the EarthScope program [*Schultz*, 2009], covering large geographic parts of the Northwest, North-Midwest, and Southeast continental United States; in a separate, smaller project, the U.S. Geological Survey (USGS) performed a magnetotelluric survey of the Florida peninsula (FL) in 2015. These surveys have been (and are being) accomplished through temporary deployments of sensor systems at various locations with an approximately 70 km spacing. At each site, geomagnetic vector data are collected using a fluxgate magnetometer, and, simultaneously, horizontal-component geoelectric vector data are collected from grounded nonpolarizable electrodes. With magnetotelluric $\mathbf{B}_h(t,x,y)$ and $\mathbf{E}_h(t,x,y)$ data, equation (2) can be solved to obtain empirical impedance tensors $\mathbf{Z}^e(\omega,x,y)$ [*Schultz et al.*, 2006–2018; *Egbert*, 2007]. These tensors are well defined across a frequency band of 10^{-4} to 10^{-1} Hz (periods of 10 to 10,000 s); errors are generally less than 5%. Empirical impedance tensors have been used to invert for 3-D models of Earth conductivity $\sigma(\mathbf{r})$ [e.g., *Bedrosian and Feucht*, 2014; *Meqbel et al.*, 2014; *Yang et al.*, 2015; *Bedrosian*, 2016], informing fundamental understanding of North American geological history and tectonic structure. A fringe benefit, not widely appreciated when the EarthScope project was initiated in 2006, is the utility of magnetotelluric data for assessing induction hazards [e.g., *Bedrosian and Love*, 2015].

A simple examination of the effect of Earth conductivity structure on induction can be made by calculating the geoelectric amplitude that would be generated by a reference geomagnetic signal. For this, we consider synthetic geomagnetic variation given by

$$\mathbf{B}_x(t) = \hat{\mathbf{x}} \cdot b_x(\omega) \cdot \sin(\omega t + \phi), \tag{4}$$

where b_x is amplitude and ϕ is phase and where $\hat{\mathbf{x}}$ is a unit vector in the north direction. In the frequency domain, this north-south geomagnetic variation gives rise to the geoelectric field

$$\mathbf{E}_h^x(\omega,x,y) = \frac{1}{\mu}\mathbf{Z}^e(\omega,x,y) \cdot \mathbf{B}_x(\omega), \tag{5}$$

where, in general, $\mathbf{E}_h^x$ is a vector field with both north E_x^x and east components E_y^x. The corresponding geoelectric amplitude is given by

$$E_h^x(\omega,x,y) = \frac{1}{\mu}\zeta_x(\omega,x,y) \cdot b_x(\omega), \tag{6}$$

where $\zeta_x = \left|\mathbf{Z}^e \cdot \hat{\mathbf{x}}\right|$ is a scalar impedance for induction driven by a north-south, sinusoidally varying geomagnetic field of frequency ω and unit amplitude, $b_x(\omega) = 1$. Similar definitions can be made for a geoelectric amplitude E_h^y generated by east-west oriented, sinusoidally varying geomagnetic field $\mathbf{B}_y$ and an impedance $\zeta_y = \left|\mathbf{Z}^e \cdot \hat{\mathbf{y}}\right|$.

Using the EarthScope and USGS empirical magnetotelluric impedances, in Figure 1, we choose to map, as an example, synthetic geoelectric amplitudes that would be induced by spatially uniform north-south $B_x(\omega)$ and east-west $B_y(\omega)$ geomagnetic variation having amplitude $b = 1$ nT and varying in time as sinusoids with period $T = 240$ s; other synthetic amplitudes can, of course, be mapped for other periodic geomagnetic variation within the frequency band of impedance resolution. Site-to-site and regional differences in the synthetic amplitudes of Figure 1 are due to local differences in impedance that, themselves, are related to interior conductivity structure. From these maps, we see that synthetic geoelectric amplitudes in the northwest are smaller than those in the Midwest and Southeast; the median amplitudes differ by about a factor of 2. In more detail, consider the Michigan Basin (MI) with its relatively thick sequence of Phanerozoic sediments on top of Proterozoic basement [e.g., *Sloss*, 1988]. For geomagnetic variation at $T = 240$ s, impedances across this region correspond to conductivities of about 10^{-2} S/m, and induced geoelectric vectors (at 240 s) are of similar amplitude [*Bedrosian*, 2016, Figure 5a]. Subsurface structure that is nearly 1-D depth dependent would give rise to such relative uniformity in synthetic geoelectric amplitudes. On the other hand, in the Archean-Superior province of northern Minnesota (MN), ancient faults and suture zones have resulted in the juxtaposition of volcanic and intrusive rocks against metasedimentary rocks [e.g., *Van Schmus and Hinze*, 1985]. Impedances (at 240 s) for this region correspond to conductivities that span 3 orders of magnitude: from 10^{-4} S/m to 10^{-1} S/m [*Bedrosian and Love*, 2015, Figure 6], and induced geoelectric vectors can have widely different amplitudes from one site to another and be strongly polarized and oriented at acute and obtuse angles relative to the inducing geomagnetic vector [*Bedrosian and Love*, 2015]. When these properties are observed across a range of frequencies, and they often are, they indicate a 3-D subsurface conductivity structure.

Independent of the EarthScope magnetotelluric survey and related modeling work, *Fernberg* [2012] used published sources to assemble simple 1-D layer model estimates of Earth conductivity for several physiographic

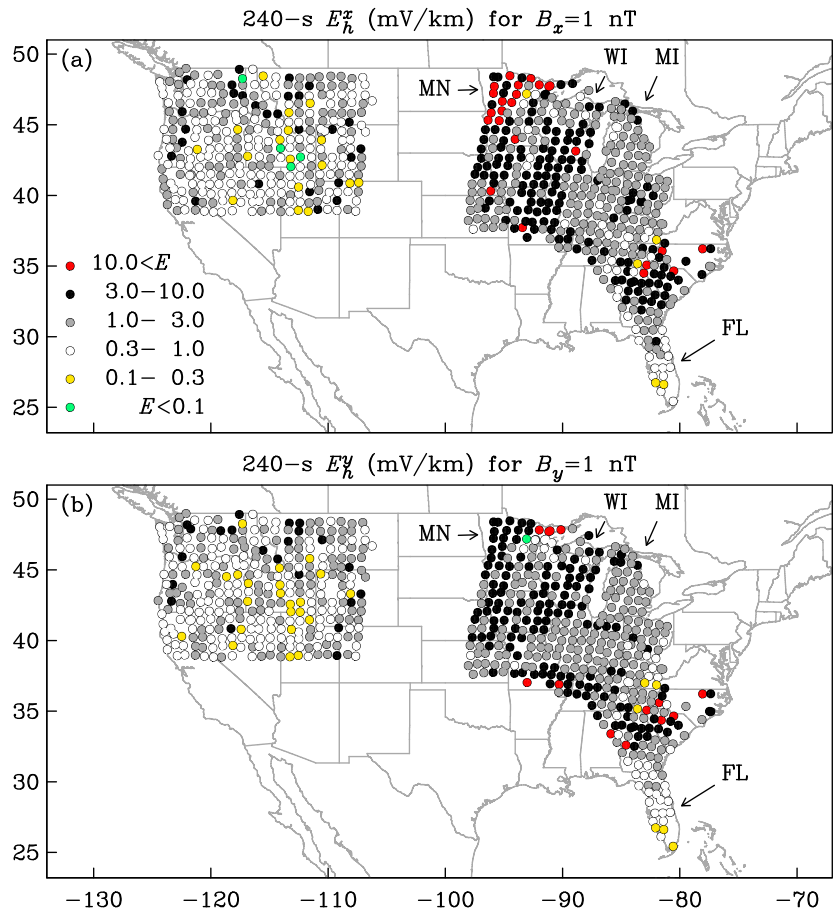

Figure 1. Maps showing synthetic geoelectric amplitudes at EarthScope and U.S. Geological Survey sites for (a) north-south and (b) east-west geomagnetic induction with an amplitude of $b(\omega) = 1$ nT and at period $T = 2\pi/\omega = 240$ s. Constructed using the methods of *Bedrosian and Love* [2015, Figure 4].

regions of the United States. His work followed from similar work done for Canada [*Ferguson and Odwar*, 1997], and it was supported by the Electric Power Research Institute and undertaken in collaboration with staff of the USGS and Natural Resources Canada. From the 1-D models, impedances can be easily calculated [*Simpson and Bahr*, 2005, chap. 2.5], and these have been used in a number of research projects [e.g., *Gannon et al.*, 2012; *Wei et al.*, 2013; *Marti et al.*, 2014; *Alekseev et al.*, 2015; *Nikitina et al.*, 2016]. The 1-D Fernberg impedances have also been used to estimate $\beta(r)$ in equation (3) for the NERC geoelectric benchmarks. But many of the physiographic regions Fernberg used encompass enormous tectonic and geological structures. One such region for the interior planes includes parts of North and South Dakota, much of Minnesota and Wisconsin, all of Iowa, Illinois, and Indiana, half of Ohio, and parts of Nebraska, Kansas, Oklahoma, and Texas (an area of approximately 500,000 km^2). This entire region is assigned a single 1-D conductivity model, and it has a single 1-D impedance tensor, based, in part, on an extrapolation of magnetotelluric measurements made in Manitoba, Canada. Many simplifying assumptions are made in Fernberg's work, and indeed, *Bedrosian and Love* [2015] have shown that their impedances do not bear much resemblance to EarthScope magnetotelluric impedances. For this reason, we are motivated to reexamine induction-hazard assessments based on Fernberg's impedances [see also *Alekseev et al.*, 2015, p. 8].

4. Sinusoidal Geomagnetic Waveforms

For many years now, geomagnetic activity has been monitored by a ground-based network of observatories [e.g., *Love*, 2008] and variometer stations [e.g., *Yumoto et al.*, 2012]. Magnetometer data from these stations show that storms are transient phenomena with activity that is distributed across a broad wash of frequencies

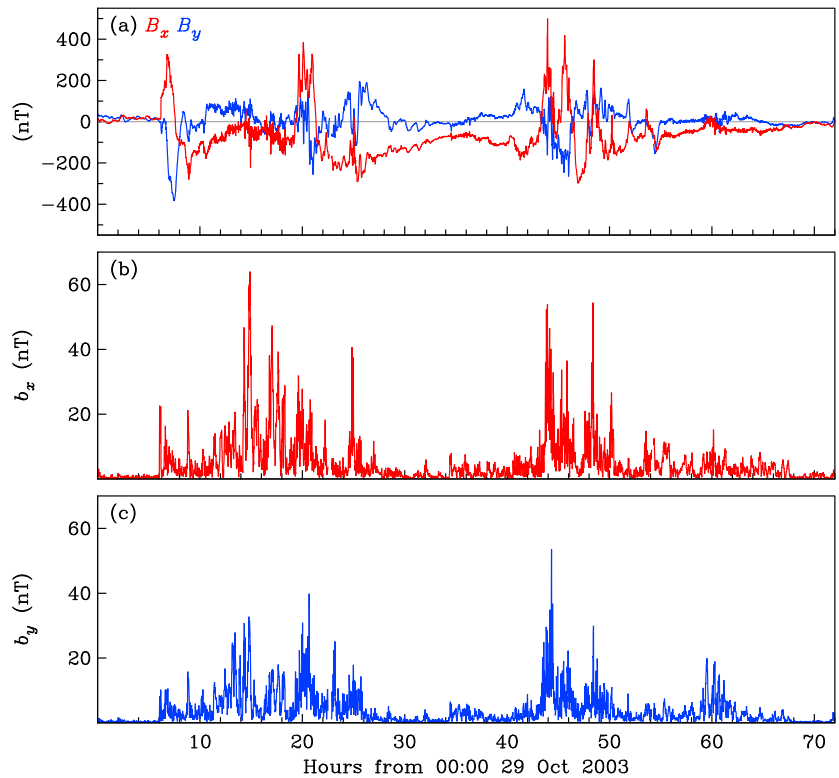

Figure 2. (a) One minute resolution, north $B_x(t)$ and east $B_y(t)$ component variation recorded at the Fredericksburg, Virginia (FRD), observatory, (38.20°N, 77.37°W) geographic, (48.62°N, 7.10°W) geomagnetic, during the Halloween storm of 29–31 October 2003. (b and c) The running amplitudes $\{b_x, b_y\}$ of $T = 2\pi/\omega = 240$ s and $W = 600$ s waveforms.

[e.g., *Olsen*, 2007], especially from about 100 s to 1000 s [e.g., *Pulkkinen and Kataoka*, 2006]. Data time series with 1 min resolution have been collected at many observatories since the 1980s and at more than a dozen observatories since the 1970s; older data are generally of 1 h resolution, and newer data are often of 1 s resolution; with the exception of only the Kakioka observatory in Japan, the duration of 1 s data collection at most observatories has been relatively short. Furthermore, the geographic distribution of long-running geomagnetic observatories is relatively sparse. The USGS, for example, operates only six observatories in the lower continental United States [*Love and Finn*, 2011]. While the present distribution of observatories is sufficient to resolve geomagnetic activity on a broad continental scale, storm-time activity can be geographically localized, especially underneath the auroral oval [e.g., *Ngwira et al.*, 2015]. One way to summarize the information content of observatory data from a sparse set of sites is to collapse statistical results across geographic latitude and longitude onto a function of geomagnetic latitude. Toward that end, we analyze 1 min resolution time series of horizontal component magnetometer data collected at 34 observatories around the world [*Love et al.*, 2016, Table 1].

The observatory data are discrete measurements in time; we represent their time stamps as $t_i, t_{i+1}, t_{i+2}, \cdots$, where $t_{i+1} - t_i$ is the 1 min (60 s) sampling interval. Sinusoidal signals with periods shorter than 2 min are squelched, in the acquisition process, by a combination of analog and digital filters. Moreover, by Nyquist's theorem, the amplitudes and phases of sinusoidal signals can only be resolved for periods longer than twice the 1 min sampling interval. Mindful of this, we take a small step away from the Nyquist limit, choosing to focus on geomagnetic variation that can be described in terms of a sinusoid having a period of 4 times the sampling interval, or $T = 2\pi/\omega = 240$ s. Recognizing that the spectral content of geomagnetic variation changes over time, especially over the course of storms, we further choose to measure the amplitude of this sinusoid over windows of length $W = 10$ min (600 s). Both of these timescales, 4 and 10 min, fall within the wide band of enhanced activity that is observed during storms. We perform a minute-by-minute running fit of the function

$$\xi(t; \mathbf{a}, \omega) = a_0 + a_1 \cdot t + a_s \cdot \sin(\omega t) + a_c \cdot \cos(\omega t), \tag{7}$$

to the north B_x and east B_y component data time series from each observatory. The parameters $\mathbf{a} = \{a_0, a_1, a_s, a_c\}$ are obtained for each t_i using a simple algorithm that minimizes the squared residual difference between ξ and 10 consecutive 1 min data values. For example, for the north B_x component, we minimize the running quantity

$$\chi^2(t_i; \mathbf{a}, \omega) = \sum_{j=1}^{10} \left[B_x(t_{i+j}) - \xi(t_{i+j}; \mathbf{a}, \omega)\right]^2; \tag{8}$$

a similar running fit is made for the east B_y component. Here a_0 is a 10 min running average, and a_1 is the slope of a linear trend in the data. The parameters a_s and a_c are amplitudes of a simple Fourier waveform; they can be combined to obtain an amplitude within a 10 min window of time,

$$b_x(t_i; \omega) = \sqrt{a_s^2 + a_c^2}. \tag{9}$$

And, again, a similar function applies for the east B_y component. Frequency resolution, here, is limited by the length of the window, $\Delta\omega \simeq 2\pi/W$. From this, it can be understood that an estimate of a given amplitude b is affected by Fourier harmonics within a relatively wide frequency band, $(\Delta\omega)/\omega \simeq T/W = 0.4$. In Figure 2a, we show geomagnetic north $B_x(t)$ and east $B_y(t)$ component variation recorded at the USGS, Fredericksburg, Virginia (FRD), observatory during the Halloween storm of October 2003. In Figures 2b and 2c we show the amplitudes $\{b_x, b_y\}$ for $T = 2\pi/\omega = 240$ s and $W = 600$ s waveforms.

5. Extreme-Value Geomagnetic Activity

The time series of waveform amplitudes $\{b_x, b_y\}$ are autocorrelated—the amplitude at one instance in time t_i is similar to the previous and subsequent value at t_{i-1} and t_{i+1}, for example. But to properly perform a statistical analysis, autocorrelation must be substantially removed. We follow *Love et al.* [2016, section 4] and "decluster" the amplitudes using a simple algorithm that gives for each observatory time series the largest waveform amplitudes within 1 day windows of time. In Figure 3a we show the cumulative probability Λ of declustered waveform amplitudes $\{b_x, b_y\}$ for FRD, 1982–2014. In modeling related data sets, power-law functions are often used [e.g., *Riley*, 2012]. We have found, however, that lognormal functions provide better fits to the $\{b_x, b_y\}$ data. And we note that since a lognormal function has a lighter tail than a power-law function, a lognormal fit to data will tend to provide a more conservative extrapolation for the cumulative number of extreme events than that provided by a power law. In Figure 3a, we show maximum likelihood, lognormal fits to the $\{b_x, b_y\}$ amplitudes. From these functions, we estimate, as extrapolations, exceedances with an average return rate of once per century (for FRD b_x, the extrapolation is to 178.8 nT; for b_y, it is to 186.7 nT).

Next, in Figure 3b, once-per-century $\{b_x, b_y\}$ exceedance values from all 34 observatories are plotted as a function of observatory geomagnetic latitude λ (this organizes geomagnetic activity better than geographic latitude). Latitude-dependent functions, represented as $\{p_x(\lambda), p_y(\lambda)\}$, are fitted to the $\{b_x, b_y\}$ exceedances. We note that the vertical axis range in both of $\{p_x, p_y\}$ is about an order of magnitude, most seen between the auroral latitude of 60° and the midlatitude of 40°. A similar latitudinal dependence is seen in the $\alpha(\lambda)$ function used in defining the *NERC* [2014, Table II-1] geoelectric amplitude benchmark. Observatory-to-observatory scatter about the fitted $p(\lambda)$ curves is noted, and we plot the (proportional) one standard deviation ($1 - \delta$, lower and upper) dispersion given by $10^{\pm\delta} \cdot p(\lambda)$; for both $\{b_x, b_y\}$, the $1 - \delta$ dispersion is approximately $[0.73, 1.36] \cdot p(\lambda)$. These results serve as reference measures of geomagnetic activity that we use for estimating geoelectric benchmarks.

Many spatiotemporal details of magnetic activity are unique for each storm [e.g., *Pulkkinen et al.*, 2006]; this simple but important point becomes obvious when working with the data used to construct Figure 3. At most observatories, geomagnetic data collected over a few decades of time record extreme-value activity that is less than that which might be expected from a statistical extrapolation of a lognormal model for once-per-century activity. But because of localized differences in geomagnetic activity realized from one storm to another, there are exceptions to this rule. For example, for data collected at the Boulder, Colorado, observatory (BOU) since 1979, amplitudes $\{b_x, b_y\}$ for the 13 March 1989 storm exceeded those that would be expected from a statistical extrapolation to once-per-century activity. As another example, since 1978, the largest waveform amplitudes $\{b_x, b_y\}$ recorded at the Barrow, Alaska (BRW), observatory occurred,

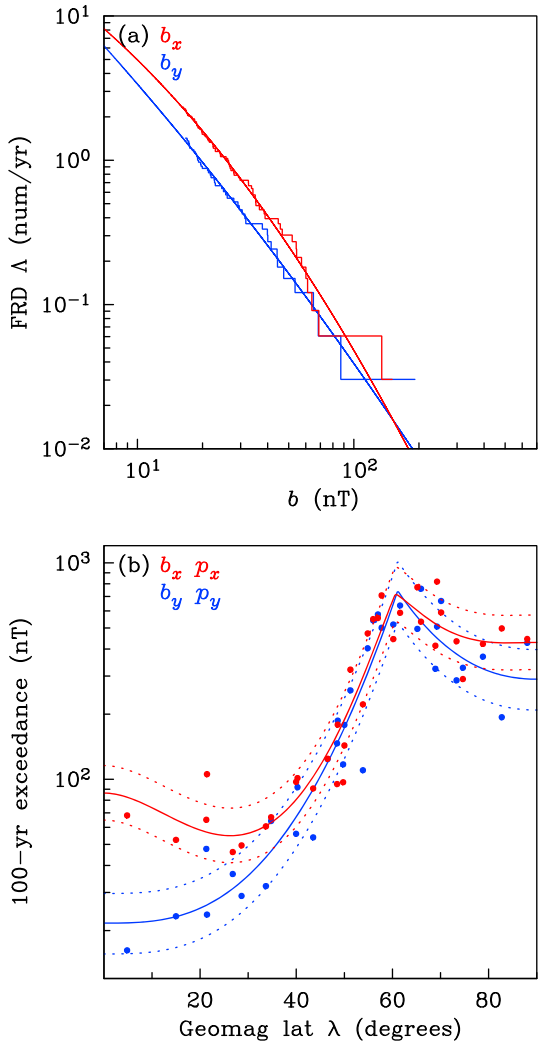

Figure 3. (a) Cumulative for declustered waveform amplitudes $\{b_x, b_y\}$ for the Fredericksburg, Virginia, magnetic observatory, 1982–2014, giving probability of the number of days per year in which activity exceeds a given threshold. (b) Once-per-century cumulative exceedances for waveform amplitudes $\{b_x, b_y\}$ from 32 observatories and functional fits to these values $\{p_x(\lambda), p_y(\lambda)\}$; dotted lines show (proportional) one standard deviation dispersion. Constructed using the methods described in *Love et al.* [2016].

respectively, on 10 September 2005 and 21 February 1994, and each during storms of modest global intensity (both amplitudes exceeded once-per-century extrapolations).

6. Extreme-Value Geoelectric Hazard Maps

In estimating extreme-value geoelectric fields, it is helpful to consider an idealized (synthetic) half-space of uniform electrical conductivity. For this, the surface impedance [e.g., *Simpson and Bahr*, 2005, chap. 2.4] can be represented as a scalar function of frequency ω and conductivity σ,

$$\frac{1}{\mu} Z(\omega, \sigma) = \sqrt{\frac{\omega}{\mu\sigma}}. \tag{10}$$

For a reference geomagnetic amplitude, we can use this to estimate an induced geoelectric amplitude,

$$E(\omega, \sigma) = \sqrt{\frac{\omega}{\mu\sigma}} \cdot b(\omega). \tag{11}$$

Analyses of historical data [*Thomson et al.*, 2011, Figure 6; *Love et al.*, 2016, Figure 4] show that geomagnetic activity at geomagnetic latitudes of $\lambda \simeq 50°$ can attain amplitudes of $b(\omega) = 250$ nT at $T = 240$ s. At a site with an effective Earth conductivity of $\sigma = 10^{-4}$ S/m (a relatively resistive value that can be realized in some geological settings), the geoelectric field would have an amplitude of about 5 V/km. This is comparable to amplitudes anticipated in other analyses using synthetic Earth conductivity models [e.g., *Kappenman*, 2003; *Ngwira et al.*, 2013].

More accurate estimates of geoelectric amplitude can be made for specific sites using the magnetotelluric impedance tensors $\mathbf{Z}^e$, which record the measured effects of Earth conductivity structure. Drawing upon the results presented in Figures 1 and 3, we can estimate the geoelectric amplitude that would be exceeded only once per century in response to extreme-intensity geomagnetic activity, $T = 240$ s and $W = 600$ s,

$$E_e(x, y) \simeq \frac{1}{\mu} \zeta(x, y) \cdot p(\lambda(x, y)). \tag{12}$$

In Figure 4 we plot, as hazard maps, the exceedances E_e^x and E_e^y, respectively, for the activity functions $\{p_x, p_y\}$. It is important to make a proper interpretation of these maps—they represent point-wise estimates of once-per-century geoelectric amplitude. In this respect, they are consistent with other types of geohazard maps, such as seismic hazard maps [e.g., *Cornell*, 1968]. The maps do not show the geoelectric amplitude that would be expected for a single, once-per-century magnetic storm. Indeed, for any given geographic location, when a once-per-century geoelectric exceedance value is realized for a particular storm, it may not be realized at another geographic location, and it is very possible that the geoelectric amplitude for the same storm, but at another location, would fall below its once-per-century exceedance value.

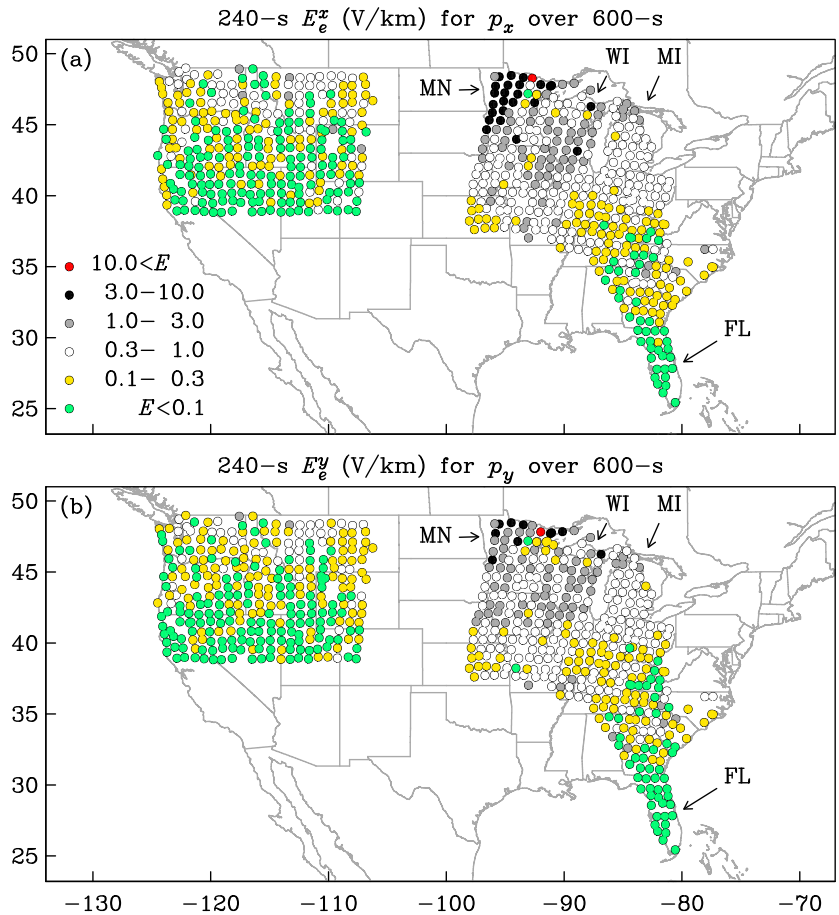

Figure 4. Maps showing maximum once-per-century geoelectric exceedances at EarthScope and U.S. Geological Survey magnetotelluric survey sites for geomagnetic induction at $T = 2\pi/\omega = 240$ s for $W = 600$ s: (a) north-south b_x; median $E_e^x = 0.26$ V/km, range [0.01, 14.00] V/km and (b) east-west; median $E_e^y = 0.23$ V/km, range [0.01, 23.35] V/km.

From Figure 4, we see that the once-per-century geoelectric amplitudes (again, for $T = 240$ s and $W = 600$ s) range over about 2 orders of magnitude (a factor of 100 or so)—this is the combined result of local site-to-site differences in impedance and the latitude dependence of geomagnetic activity. Within regions of the United States where a magnetotelluric survey was completed, Minnesota (MN) and Wisconsin (WI) have some of the highest geoelectric hazards, while Florida (FL) has some of the lowest. Among all the survey sites, once-per-century, north-south geomagnetic activity b_x induces geoelectric amplitudes E_e^x with a median value of 0.26 V/km; for once-per-century east-west geomagnetic activity, the geoelectric amplitudes E_e^y have a median value of 0.23 V/km; these values are much less than the typical 5 V/km value in the *NERC* [2014, pp. 23–24] benchmark. However, Figure 4 shows us that storm-time geoelectric amplitudes are an intricate function of geographic location. At many sites in the United States, once-per-century geoelectric amplitudes are comparable to the 1 min resolution value of ~ 0.4 V/km measured at Kakioka, Japan (KAK), during the sudden commencement event of 24 March 1991. Across the northern Midwest of the United States, once-per-century geoelectric amplitudes exceed the 2 V/km that *Boteler* [1994] has inferred was responsible for bringing down the Hydro-Québec electric-power grid in Canada in March 1989.

The survey site with the largest scalar impedance for 240 s, north-south induction (MNB36) is located in northern Minnesota, (48.27°N, 92.71°W) geographic, (58.03°N, 27.16°W) geomagnetic; here once-per-century north-south induction b_x generates a geoelectric amplitude E_e^x of 14.00 V/km. The survey site with the largest impedance for 240 s, east-west induction (MNC37) is also located in northern Minnesota, (47.83°N, 91.99°W) geographic, (57.64°N, 26.16°W) geomagnetic; here once-per-century east-west induction b_y generates a geoelectric amplitude E_e^y of 23.35 V/km. But just 123 km away, at another site (RED36), (47.19°N, 93.07°W) geographic, (56.92°N, 27.35°W) geomagnetic, once-per-century b_x and b_y induction generates geoelectric

amplitudes of only 0.08 and 0.02 V/km. In each of these cases, as discussed in section 5, we estimate the statistical $1-\delta$ dispersion of individual geoelectric amplitudes as being approximately $[0.73, 1.36] \cdot E_h$. An estimate [*Anderson et al.*, 1974] that geoelectric amplitudes could have reached $\sim$ 7 V/km at 10^{-2} Hz during the magnetic storm of 4 August 1972, obtained for a synthetic, 1-D Earth conductivity model for Illinois, would seem to exceed a once-per-century threshold for that part of the country, though the occurrence of such an amplitude there cannot be simply dismissed on statistical grounds.

7. Discussion

Looking beyond the simple parameterization of induction adopted here, scenario maps of induced geoelectric fields can be produced by mapping geomagnetic activity, obtained by fitting model basis functions to ground magnetometer data [e.g., *Pulkkinen et al.*, 2003; *Rigler et al.*, 2014], and convolving them, for a broad band of frequencies, with maps of Earth surface impedance, obtained by inverse modeling of magnetotelluric survey data. If long, multidecade observatory time series are used for such calculations, the geoelectric field outputs can be analyzed statistically — obtaining an improvement over the hazard assessment presented here. This work highlights the need for completing the national magnetotelluric survey and for additional geomagnetic monitoring stations to complete (and improve) assessments of geoelectric hazards for the continental United States. For this, a high-priority area is the northeast United States, a region that includes several major metropolitan centers and corresponding electric-power grid infrastructure, all of which are situated on top of complicated geological and tectonic structures and at latitudes where geomagnetic activity can be locally intense. In some areas, such as in northern Minnesota (MN) where local geological and tectonic structure evidently results in geoelectric fields of great geographic complexity, detailed magnetotelluric surveys might be necessary. Additional geomagnetic monitoring and a magnetotelluric survey of southern Canada would lead to improved hazard mapping in the Northern United States, and it would enable risk assessment of integrated North American continental, electric-power grid networks.

Acknowledgments
We thank J. Campanyá, A.D. Chave, J. McCarthy, R. Sharma, J.L. Slate, A. Veeramany, and J.R. Woodroffe for reviewing a draft manuscript. We thank E.E. Bernabeu, W.S. Leith, and W. Murtagh for their useful conversations. Magnetic observatory data were obtained from either the Kyoto or Edinburgh World Data Centers or from INTERMAGNET. We thank the national institutes that support the operation of magnetic observatories and INTERMAGNET for promoting high standards of observatory practice (www.intermagnet.org). Geoelectric data can be obtained from the Kakioka Magnetic Observatory. EarthScope impedance tensors can be obtained from the Data Management Center of the Incorporated Research Institutions for Seismology (ds.iris.edu/ds/products/emtf). Views expressed in this paper do not necessarily represent those of FERC.

References

Alekseev, D., A. Kuvshinov, and N. Palshin (2015), Compilation of 3D global conductivity model of the Earth for space weather applications, *Earth Planets Space*, *67*, 108, doi:10.1186/s40623-015-0272-5.
Allen, J., L. Frank, H. Sauer, and P. Reiff (1989), Effects of the March 1989 solar activity, *Eos Trans. AGU*, *70*(46), 1479, 1486–1488.
Anderson, C. W., L. J. Lanzerotti, and G. MacLennan (1974), Outage of the L4 System and the geomagnetic disturbances of 4 August 1972, *Bell Syst. Tech. J.*, *53*(9), 1817–1837.
Aon Benfield (2013), *Geomagnetic Storms*, pp. 1–12, Aon Benfield, Sydney, Australia.
Baker, D. N., et al. (2008), *Severe Space Weather Events — Understanding Societal and Economic Impacts*, pp. 1–144, National Academy Press, Washington, D. C.
Bedrosian, P. A. (2016), Making it and breaking it in the Midwest: Continental assembly and rifting from modeling of EarthScope magnetotelluric data, *Precambrian Res.*, *278*, 378–361, doi:10.1016/j.precamres.2016.03.009.
Bedrosian, P. A., and D. W. Feucht (2014), Structure and tectonics of the northwestern United States from EarthScope USArray magnetotelluric data, *Earth Planet. Sci. Lett.*, *402*, 275–289, doi:10.1016/j.epsl.2013.07.035.
Bedrosian, P. A., and J. J. Love (2015), Mapping geoelectric fields during magnetic storms: Synthetic analysis of empirical United States impedances, *Geophys. Res. Lett.*, *42*(23), 10,160–10,170, doi:10.1002/2015GL066636.
Béland, J., and K. Small (2005), Space weather effects on power transmission systems: The cases of Hydro-Québec and Transpower New Zealand Ltd, in *Effects of Space Weather on Technology Infrastructure*, edited by I. A. Daglis, pp. 287–299, Springer, Dordrecht, Neth.
Bolduc, L. (2002), GIC observations and studies in the Hydro-Québec power system, *J. Atmos. Sol. Terr. Phys.*, *64*, 1793–1802.
Boteler, D. H. (1994), Geomagnetically induced currents: Present knowledge and future research, *IEEE Trans. Power Delivery*, *9*(1), 50–58.
Burstinghaus, E. J., T. K. Saha, R. A. Marshall, and K. Yumoto (2013), The importance of non-uniform geoelectric fields in calculating GIC distributions, in *IEEE Power Energy Society General Meeting*, pp. 1–5, IEEE, Vancouver, BC., doi:10.1109/PESMG.2013.6672289
Cannon, P., et al. (2013), *Extreme Space Weather: Impacts on Engineered Systems and Infrastructure*, pp. 1–68, Roy. Acad. Engineer., London.
Cornell, A. (1968), Engineering seismic risk analysis, *Bull. Seismol. Soc. Am.*, *58*(5), 1583–1606.
Egbert, G. D. (2007), Robust electromagnetic transfer functions estimates, in *Encyclopedia of Geomagnetism and Paleomagnetism*, edited by D. Gubbins and E. Herrero-Bervera, pp. 866–870, Springer, Dordrecht, Neth.
Federal Energy Regulatory Commission (2013), Reliability standards for geomagnetic disturbances, Fed. Energy Reg. Comm., *Fed. Reg. Rules Regulations*, *78*(100), 30,747–30,762.
Ferguson, I. J., and H. D. Odwar (1997), Review of conductivity soundings in Canada, Appendix 3, in *Geomagnetically Induced Currents: Geomagnetic Hazard Assessment, Phase II, 357 T 848A*, vol. 3, edited by D. H. Boteler, pp. 1–121, Geol. Surv. Canada and Canadian Electr. Assoc., Ottawa.
Fernberg, P. (2012), *One-Dimensional Earth Resistivity Models for Selected Areas of Continental United States and Alaska*, pp. 1–190, EPRI Technical Update 1026430, Palo Alto, Calif.
Gannon, J. L., L. Trichtchenko, and P. Fernberg (2012), United States regional GIC hazard assessment, Abstract SM21D-08 presented at 2012 Fall Meeting, AGU, San Francisco, Calif., 3–7 Dec.
Kappenman, J. G. (2003), Storm sudden commencement events and the associated geomagnetically induced current risks to ground-based systems at low-latitude and midlatitude locations, *Space Weather*, *1*, 1016, doi:10.1029/2003SW000009.
Kappenman, J. G. (2012), A perfect storm of planetary proportions, *IEEE Spectrum*, *49*, 26–31.
Lloyd's (2013), *Emerging Risk Report: Solar Storm Risk to the North American Electric Grid*, pp. 1–22, Lloyd's of London, London, U. K.

Love, J. J. (2008), Magnetic monitoring of Earth and space, *Phys. Today*, *61*(2), 31–37, doi:10.1063/1.2883907.
Love, J. J., and C. A. Finn (2011), The USGS Geomagnetism Program and its role in space weather monitoring, *Space Weather*, *9*, S07001, doi:10.1029/2011SW000684.
Love, J. J., E. J. Rigler, A. Pulkkinen, and C. C. Balch (2014), Magnetic storms and induction hazards, *Eos Trans. AGU*, *95*(48), 445–446, doi:10.1002/2014EO480001.
Love, J. J., P. Coïsson, and A. Pulkkinen (2016), Global statistical maps of extreme-event magnetic observatory 1-min first differences in horizontal intensity, *Geophys. Res. Lett.*, *43*, 4126–4135, doi:10.1002/2016GL068664.
Marti, L., C. Yiu, A. Rezaei-Zare, and D. Boteler (2014), Simulation of geomagnetically induced currents with piecewise layered-Earth models, *IEEE Trans. Power Delivery*, *29*, 1186–1193, doi:10.1109/TPWRD.2014.2317851.
Meqbel, N. M., G. D. Egbert, P. E. Wannamaker, A. Kelbert, and A. Schultz (2014), Deep electrical resistivity structure of the northwestern U.S. derived from 3-D inversion of USArray magnetotelluric data, *Earth Planet. Sci. Lett.*, *402*, 290–304, doi:10.1016/j.epsl.2013.12.026.
Molinski, T. S. (2002), Why utilities respect geomagnetically induced currents, *J. Atmos. Sol. Terr. Phys.*, *64*, 1765–1778.
NERC (2014), *Benchmark Geomagnetic Disturbance Event Description*, pp. 1–26, North Am. Electric Reliability Corp., Atlanta, Ga.
Ngwira, C. M., A. Pulkkinen, F. D. Wilder, and G. Crowley (2013), Extended study of extreme geoelectric field event scenarios for geomagnetically induced current applications, *Space Weather*, *11*, 121–131, doi:10.1002/swe.20021.
Ngwira, C. M., A. A. Pulkkinen, E. Bernabeu, J. Eichner, A. Viljanen, and G. Crowley (2015), Characteristics of extreme geoelectric fields and their possible causes: Localized peak enhancements, *Geophys. Res. Lett.*, *42*, 6916–6921, doi:10.1002/2015GL065061.
Nikitina, L., L. Trichtchenko, and D. Boteler (2016), Assessment of extreme values in geomagnetic and geoelectric field variations for Canada, *Space Weather*, *14*, 481–494, doi:10.1002/2016SW001386.
National Science and Technology Council (2015), *National Space Weather Strategy*, pp. 1–13, Executive Office, National Sci. Tech. Council, Washington, D. C.
Olsen, N. (2007), Natural sources for electromagnetic induction studies, in *Encyclopedia of Geomagnetism and Paleomagnetism*, edited by D. Gubbins and E. Herrero-Bervera, pp. 743–746, Springer, Dordrecht, Neth.
Overbye, T. J., T. R. Hutchins, K. Shetye, J. Weber, and S. Daham (2012), Integration of geomagnetic disturbance modeling into the power flow: A methodology for large-scale system studies, in *North American Power Symposium*, pp. 1–7., Univ. of Illinois, Urbana-Champaign, Ill., doi:10.1109/NAPS.2012.6336365.
Piccinelli, R., and E. Krausmann (2014), *Space Weather and Power Grids—A Vulnerability Assessment*, pp. 1–53, European Union, Luxembourg.
Pulkkinen, A. (2015), Geomagnetically induced currents modeling and forecasting, *Space Weather*, *13*, 734–736, doi:10.1002/2015SW001316.
Pulkkinen, A., and R. Kataoka (2006), S-transform view of geomagnetically induced currents during geomagnetic superstorms, *Geophys. Res. Lett.*, *33*, L12108, doi:10.1029/2006GL025822.
Pulkkinen, A., O. Amm, A. Viljanen, and BEAR working group (2003), Ionospheric equivalent current distributions determined with the method of spherical elementary current systems, *J. Geophys. Res.*, *108*(A2), 1053, doi:10.1029/2001JA005085.
Pulkkinen, A., S. Lindahl, A. Viljanen, and R. Pirjola (2005), Geomagnetic storm of 29–31 October 2003: Geomagnetically induced currents and their relation to problems in the Swedish high-voltage power transmission system, *Space Weather*, *3*, S08C03, doi:10.1029/2004SW000123.
Pulkkinen, A., A. Klimas, D. Vassiliadis, V. Uritsky, and E. Tanskanen (2006), Spatiotemporal scaling properties of the ground geomagnetic field variations, *J. Geophys. Res.*, *111*, A03305, doi:10.1029/2005JA011294.
Rigler, E. J., A. A. Pulkkinen, C. C. Balch, and M. J. Wiltberger (2014), *Dynamic geomagnetic hazard maps in space weather operations*, AGU, San Francisco, Calif., 15–19 Dec.
Riley, P. (2012), On the probability of occurrence of extreme space weather events, *Space Weather*, *10*, S02012, doi:10.1029/2011SW000734.
Schrijver, C. J., et al. (2015), Understanding space weather to shield society: A global road map for 2015–2025 commissioned by COSPAR and ILWS, *Adv. Space Res.*, *55*(12), 2745–2807, doi:10.1016/j.asr.2015.03.023.
Schultz, A. (2009), *A continental scale magnetotelluric observatory and data discovery resource*, vol. 8, IGY6–IGY20.
Schultz, A., G. D. Egbert, A. Kelbert, T. Peery, V. Clote, B. Fry, S. Erofeeva, and staff of the National Geoelectromagnetic Facility and their contractors (2006–2018), USArray TA magnetotelluric transfer functions, doi:10.17611/DP/EMTF/USARRAY/TA.
Simpson, F., and K. Bahr (2005), *Practical Magnetotellurics*, pp. 1–254, Cambridge Univ. Press, Cambridge, U. K.
Sloss, L. L. (1988), Tectonic evolution of the craton in Phanerozoic time, in *Sedimentary Cover—North American Craton: U.S., chap. 3*, vol. D-2, edited by L. L. Sloss, pp. 25–52, Geol. Soc. Am., Boulder, Colo.
Stratton, J. A. (1941), *Electromagnetic Theory*, pp. 1–615, McGraw-Hill Book Company, New York.
Thomson, A. W. P. (2007), Geomagnetic hazards, in *Encyclopedia of Geomagnetism and Paleomagnetism*, edited by D. Gubbins and E. Herrero-Bervera, pp. 316–319, Springer, Dordrecht, Neth.
Thomson, A. W. P., A. J. McKay, E. Clarke, and S. J. Reay (2005), Surface electric fields and geomagnetically induced currents in the Scottish Power grid during the 30 October 2003 geomagnetic storm, *Space Weather*, *3*, S11002, doi:10.1029/2005SW000156.
Thomson, A. W. P., E. B. Dawson, and S. J. Reay (2011), Quantifying extreme behavior in geomagnetic activity, *Space Weather*, *9*, S10001, doi:10.1029/2011SW000696.
Torta, J. M., S. Marsal, and M. Quintana (2014), Assessing the hazard from geomagnetically induced currents to the entire high-voltage power network in Spain, *Earth Planets Space*, *66*, 87, doi:10.1186/1880-5981-66-87.
Unsworth, M. (2007), Magnetotellurics, in *Encyclopedia of Geomagnetism and Paleomagnetism*, edited by D. Gubbins and E. Herrero-Bervera, pp. 670–673, Springer, Dordrecht, Neth.
Van Schmus, W. R., and W. J. Hinze (1985), The midcontinent rift system, *Ann. Rev. Earth Planet. Sci.*, *13*, 345–383.
Veeramany, A., S. D. Unwin, G. A. Coles, J. E. Dagle, D. W. Millard, J. Yao, C. S. Glantz, and S. N. G. Gourisetti (2016), Framework for modeling high-impact, low-frequency power grid events to support risk-informed decisions, *Int. J. Disaster Risk Reduction*, *18*, 125–137, doi:10.1016/j.ijdrr.2016.06.008.
Wei, L. H., N. Homeier, and J. L. Gannon (2013), Surface electric fields for North America during historical geomagnetic storms, *Space Weather*, *11*, 451–462, doi:10.1002/swe.20073.
Yang, B., G. D. Egbert, A. Kelbert, and N. M. Meqbel (2015), Three-dimensional electrical resistivity of the north-central USA from EarthScope long period magnetotelluric data, *Earth Planet. Sci. Lett.*, *422*, 87–93.
Yumoto, K., et al. (2012), ULTIMA: Array of ground-based magnetometer arrays for monitoring magnetospheric and ionospheric perturbations on a global scale, *Abstract SM14A-01 presented at Fall Meeting*, AGU, San Francisco, Calif., 3–7 Dec.
Zheng, K., L. Trichtchenko, R. Pirjola, and L. G. Liu (2013), Effects of geophysical parameters on GIC illustrated by benchmark network modeling, *IEEE Trans. Power Delivery*, *28*, 1183–1191, doi:10.1109/TPWRD.2013.2249119.